RESEARCH LETTER

Key Points:
- We used geophysical methods to image shallow degassing in a Yellowstone hydrothermal system
- Electrical resistivity, seismic velocity, and Poisson's ratio provide robust images to map shallow plumbing systems
- Rock physics modeling supports our interpretation and provides critical insight to understand hydrothermal systems

Geophysical imaging of shallow degassing in a Yellowstone hydrothermal system

S. Pasquet[1,2], W. S. Holbrook[1,2], B. J. Carr[1,2], and K. W. W. Sims[1]

[1]Department of Geology and Geophysics, University of Wyoming, Laramie, Wyoming, USA, [2]Wyoming Center for Environmental Hydrology and Geophysics, University of Wyoming, Laramie, Wyoming, USA

Abstract The Yellowstone Plateau Volcanic Field, which hosts over 10,000 thermal features, is the world's largest active continental hydrothermal system, yet very little is known about the shallow "plumbing" system connecting hydrothermal reservoirs to surface features. Here we present the results of geophysical investigations of shallow hydrothermal degassing in Yellowstone. We measured electrical resistivity, compressional-wave velocity from refraction data, and shear wave velocity from surface-wave analysis to image shallow hydrothermal degassing to depths of 15–30 m. We find that resistivity helps identify fluid pathways and that Poisson's ratio shows good sensitivity to saturation variations, highlighting gas-saturated areas and the local water table. Porosity and saturation predicted from rock physics modeling provide critical insight to estimate the fluid phase separation depth and understand the structure of hydrothermal systems. Finally, our results show that Poisson's ratio can effectively discriminate gas- from water-saturated zones in hydrothermal systems.

1. Introduction

The Yellowstone Plateau Volcanic Field (YPVF) is the world's largest active continental hydrothermal system, with over 10,000 thermal features including geysers, fumaroles, mud pots and hot springs [*Fournier*, 1989; *Lowenstern and Hurwitz*, 2008; *Hurwitz and Lowenstern*, 2014]. Numerous seismic studies have investigated the deep origins of this activity, highlighting the existence of a large reservoir of silicic magma in the shallow crust [*Benz and Smith*, 1984; *Miller and Smith*, 1999; *Husen et al.*, 2004; *Chu et al.*, 2010; *Farrell et al.*, 2014; *Huang et al.*, 2015]. The presence of this reservoir has led to three cataclysmic volcanic eruptions over the past 2.1 Ma, the latest (~0.631 Ma) causing the formation of the 2900 km^2 large Yellowstone caldera [*Christiansen*, 2001; *Matthews et al.*, 2015]. Most of the hydrothermal features observed in Yellowstone are located within this caldera and can be divided into two main groups based on their fluid composition [*White et al.*, 1971]. On the one hand, neutral-chloride water thermal features, mainly found in the western part of the caldera, are characterized by siliceous sinter deposition and clear water. On the other hand, vapor-dominated, acid-sulfate thermal areas are usually characterized by fumaroles and mud pots and are mostly located in the eastern half of the caldera, where seismic tomography suggests that magma is closest to the surface [*Farrell et al.*, 2014].

While the temporal and spatial variabilities of these hydrothermal features have been studied in extensive surface investigations [*White et al.*, 1971; *Fournier*, 1989; *Werner et al.*, 2000; *Werner and Brantley*, 2003; *Hurwitz et al.*, 2007, 2012; *Lowenstern et al.*, 2012], very little is known about the "plumbing" system connecting these surface features to deeper reservoirs of hydrothermal fluids. Information about the depth of liquid-gas phase separation and the pathways followed by these fluids toward the surface is critical to understand the formation and evolution of the different hydrothermal features observed in YPVF. Knowledge of fluid pathways and subsurface physical properties would enable improved understanding of the depths of separation of steam from liquid water [*White et al.*, 1971; *Fournier*, 1989], the large-scale hydrological flow paths that connect meteoric water to the hydrothermal systems [*Vitale et al.*, 2008], the controls of geology and fracture systems on the location and chemistry of the hot springs [*Morgan and Shanks*, 2005; *Hurwitz and Lowenstern*, 2014], and the source reservoirs of fluids that feed the diverse microbial communities that colonize the surface springs [*Shock et al.*, 2005; *Dick and Shock*, 2011, 2013; *Boyd et al.*, 2012; *Dick and Shock*, 2013]. Moreover, while several studies have proposed conceptual models or cartoons of subsurface hydrothermal systems [e.g., *White et al.*, 1971; *Gibson and Hinman*, 2013], those models are often based on inference and geological reasoning and are seldom constrained by subsurface data. Since drilling in these sensitive hydrothermal areas is rare, near-surface geophysical techniques are generally the only available options to image the shallow subsurface

(<100 m). Although near-surface geophysical studies are increasingly common to image flow paths of hydrothermal fluids in geothermal systems [*Revil et al.*, 2004, 2008; *Bruno et al.*, 2007; *Finizola et al.*, 2010; *Byrdina et al.*, 2014; *Rosas-Carbajal et al.*, 2016], they have rarely been applied in Yellowstone [*Zohdy et al.*, 1973; *Vandemeulebrouck et al.*, 2013, 2014].

We present here the results of geophysical investigations of shallow degassing in the vapor-dominated, acid-sulfate Obsidian Pool Thermal Area (OPTA) in the eastern part of the Yellowstone caldera. In addition to the widely used electrical methods, we propose a methodology combining seismic refraction and surface-wave profiling to estimate both compressional (*P*) and shear (*S*) wave velocities, and thereby Poisson's ratio [*Pasquet et al.*, 2015b]. Our work is unique in applying a rock physics model, based on Hertz-Mindlin contact theory [*Mindlin*, 1949], to quantitatively predict subsurface porosity and saturation from seismic velocities in a shallow hydrothermal system. We find that seismic velocity and electrical resistivity data provide robust images of fluid and gas pathways and that Poisson's ratio provides good first-order constraints on gas and water saturation at depth. Furthermore, porosity and saturation predicted from rock physics modeling provide critical insight to understand the structure of hydrothermal systems and indicate that the phase separation between hydrothermal fluids occurs at least 15 m in depth.

2. Site Description

The Obsidian Pool Thermal Area (also referred in the literature as Greater Obsidian Pool Area; Figure 1) is located in the eastern part of the Yellowstone caldera, within the Mud Volcano thermal area, just southwest of a lake referred to as Goose Lake in *Werner et al.* [2000]. The Mud Volcano thermal area mainly consists of rhyolitic ash flow tuff covered with varying thicknesses of glacial silts, sand, and gravel [*Christiansen and Blank*, 1975]. In the Y-11 borehole drilled in the area by the U.S. Geological Survey, rhyolitic ash flow tuffs are covered with approximately 18 m of fluvial sediments and glacial tills, mostly of rhyolitic composition [*Bargar and Muffler*, 1982]. The area is characterized by extensive diffuse degassing of CO_2 through soils [*Werner et al.*, 2000; *Werner and Brantley*, 2003] and hosts several isolated thermal features. Though thermal features characteristic of liquid-dominated systems have been observed in OPTA [*Meyer-Dombard et al.*, 2005], thermal pools present in the area are mostly characterized by acid-sulfate composition and have water temperatures between 21.9°C and 84.0°C [*Hurwitz et al.*, 2012]. All of the pools are bubbling and have temperatures below the boiling point of water, suggesting a strong influx of CO_2-rich gas. An intense degassing feature (hereafter referred as the "frying pan") in the southern part of the area (Figure 1b) is located at the center of a 50 × 80 m heat flow anomaly previously highlighted by *Hurwitz et al.* [2012] and clearly delineated by bare soils with no snow accumulation or vegetation. The active part of the feature is approximately 10 × 10 m and shows visible degassing, with a small proportion of water bubbling at the surface with a temperature of 89.0°C.

3. Data Acquisition, Processing, and Results

We collected geophysical data in November 2015 along a 380 m SSW-NNE transect, crossing the heat flow anomaly between 50 and 120 m, the frying pan degassing feature between 86 and 96 m, and an acid-sulfate thermal pool (hereafter referred as the "figure-eight" pool) between 245 and 260 m (Figure 1b). The hydrothermal features and the acquisition line were GPS surveyed, and the topography was extracted from airborne lidar data available in the area (http://www.opentopography.org).

3.1. Electrical Resistivity Survey

We performed electrical resistivity tomography (ERT) along this transect by using an eight-channel resistivity meter with a mixed array composed of extended dipole-dipole and strong gradient arrays. Reciprocal measurements were collected and totaled 15% of the data volume. The system was set up in two deployments of 112 electrodes at 2 m intervals with an overlap of 56 electrodes to create a 334 m long profile. For the seven electrode positions located in the figure-eight pool, electrical current was injected directly from the water-immersed electrode take-outs. Measurement errors were estimated by describing the absolute reciprocal error as a function of resistance [*Koestel et al.*, 2008]. Apparent electrical resistivity data were then inverted for true electrical resistivity (ρ) structure by using the R2 software package (http://www.es.lancs.ac.uk/people/amb/Freeware/R2/R2.htm) [*Binley and Kemna*, 2005]. Finally, the depth of investigation (DOI) of the final model was estimated by using the DOI index [*Oldenburg*
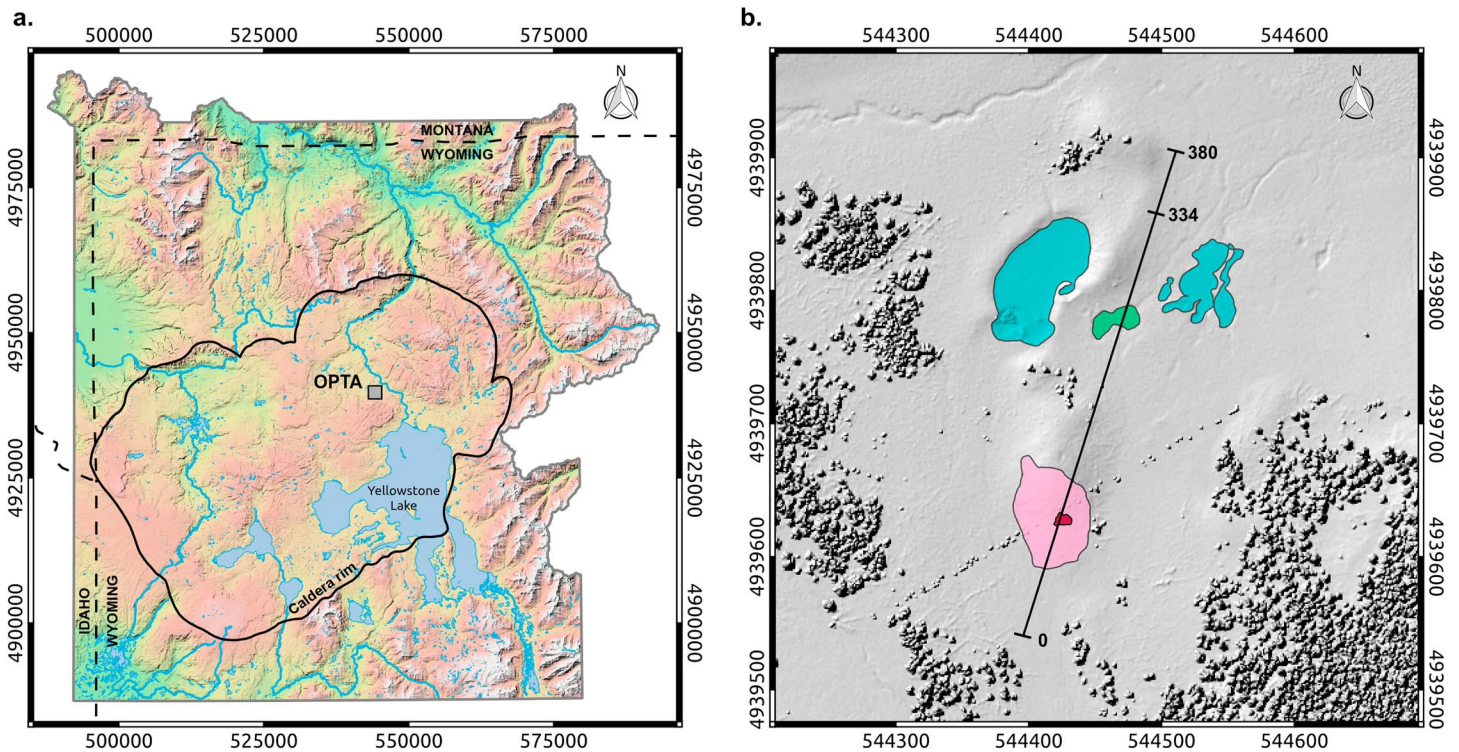
Figure 1. (a) Shaded-relief topographic map of Yellowstone National Park showing the rim of Yellowstone caldera (solid black line), national park boundary (solid gray line), and state boundaries (dashed black line). The Obsidian Pool Thermal Area (OPTA) is marked with a gray square. (b) High-resolution lidar shaded-relief topographic map of the OPTA showing the figure-eight pool (shaded green area), the neighboring thermal pools (shaded blue areas), the heat flow anomaly surrounding the frying pan (shaded pink area), the frying pan degassing feature (shaded red area), and the acquisition line (solid black line) with specific markers at 334 m and 380 m corresponding to the extent of the resistivity and seismic surveys, respectively. Both maps are projected in the Universal Transverse Mercator geographic coordinate system, zone 12 N.

and Li, 1999], which quantifies the depth at which electrical resistivity measurements become insensitive to changes in a reference model.

The inverted resistivity model (Figure 2a) shows ρ values ranging from 4 to 4000 Ωm, with a maximum investigation depth of about 25 m. Shallow higher resistivity values (down to ~8 m deep) are visible in the most elevated part of the line (from 70 to 220 m). A more conductive body is present between 190 m and the end of the line, connecting with the surface at the location of the figure-eight pool. An intermediate resistivity area between 180 and 230 m seems to separate the pools and the frying pan, the latter being characterized by a shallow resistive area, followed at depth by lower resistivity values.

3.2. Seismic Refraction and Surface-Wave Survey

We acquired seismic data by using eight 24-channel seismic recorders and 192 10 Hz vertical component geophones spaced at 2 m, with a 5.4 kg sledgehammer source striking a metal plate every 10 m, so as to obtain a 382 m long profile having the same origin as the ERT profile. For obvious reasons, we could use neither the source nor the geophones in the figure-eight pool, leading to a data gap between 245 and 260 m.

First arrival times were picked manually on the seismograms and inverted for *P* wave velocity (V_P) by using a MATLAB travel time tomography code [*St. Clair*, 2015]. In order to estimate the sensitivity and the depth of investigation of our model, we repeated the inversions for a range of 50 starting models with different velocity gradients and surface velocities. All models presenting a satisfactory fit to the data were used to build an average final model with a depth of investigation defined by using the standard deviation of all selected models.

The *P* wave velocity model (Figure 2b) shows V_P smoothly ranging between 200 m/s and 2200 m/s, with an investigation depth of about 30 m. An ~5 m thick, low-velocity layer present at the surface is
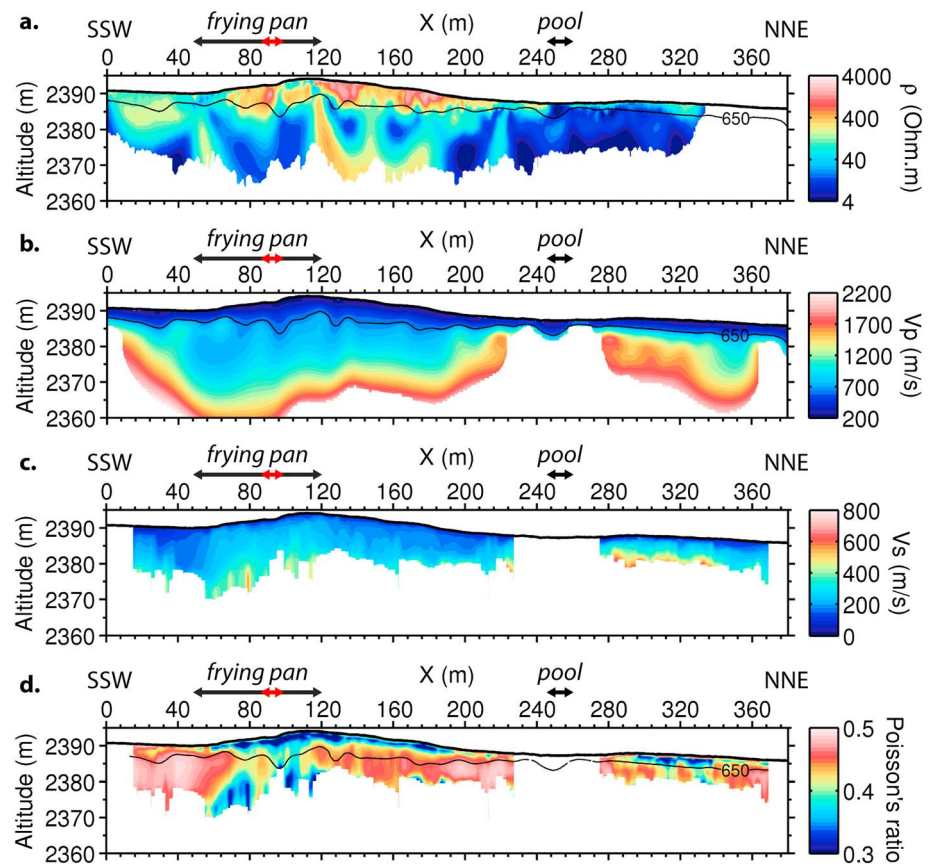
Figure 2. (a) Electrical resistivity (ρ) model obtained from electrical resistivity tomography. (b) P wave velocity (V_P) model obtained from travel time tomography. (c) S wave velocity (V_S) model obtained from surface-wave profiling. (d) Poisson's ratio model computed from V_P and V_S. The topography extracted from airborne lidar data is represented with a black solid line. The location of the figure-eight pool and the heat flow anomaly are represented with black arrows, while the active part of the frying pan is represented with a red arrow. The black contour line in Figures 2a, 2b, and 2d corresponds to a constant V_P of 650 m/s.

coincident with the shallow resistive layer in the ERT model beneath the hill. While the NNE part is characterized by a rapid increase of V_P, the SSW part shows lower velocities, especially below the frying pan. A large gap corresponding to the figure-eight pool is present in the model due to the small number of identified first arrivals when the shot and the traces were located on opposite sides of the pool. Indeed, signal-to-noise ratio was very low around the figure-eight pool due to active cavitation of large bubbles in the pool.

The seismic data were also processed to perform surface-wave profiling by using the SWIP software package (https://github.com/SWIPdev/SWIP/releases) [*Pasquet and Bodet*, 2016]. Surface-wave dispersion was computed along the acquisition profile by using windowing and stacking techniques, so as to obtain a set of 179 dispersion images. On each dispersion image, the coherent maxima associated with the different propagation modes were identified, picked, and extracted with an estimated standard error in phase velocity. Assuming a 1-D tabular medium, we performed Monte Carlo inversions of the dispersion curves picked at each window position to obtain a set of consecutive 1-D S wave velocity (V_S) models. For each position along the line, models matching the observed data within the error bars were selected to build a misfit-weighted final model and estimate the investigation depth. Finally, each 1-D V_S model was represented at its corresponding extraction position to create a 2-D V_S section.

The S wave velocity model (Figure 2c) is characterized by V_S values varying between 50 m/s and 800 m/s, with an investigation depth ranging between 10 and 15 m. Higher shallow velocities are present on the NNE side of the figure-eight pool and under the frying pan. Although the V_S model has a low

investigation depth, it provides more information regarding the lateral variations of shallow layers' velocities than the V_P model, due to the large horizontal component of P wave travel paths and the smoothing inherent in P wave tomographic inversion.

In order to constrain the presence of hydrothermal fluids, we used Poisson's ratio, which is known to be a good indicator of water saturation changes in the subsurface [*Pasquet et al.*, 2015a]. Using the inverted V_P and V_S models, we computed Poisson's ratio as

$$v = \frac{V_P{}^2 - 2V_S{}^2}{2\left(V_P{}^2 - V_S{}^2\right)} \tag{1}$$

The inferred Poisson's ratio (Figure 2d) shows values ranging from 0.3 to 0.5, which are typical of nonsaturated and saturated media, respectively. The Poisson's ratio is predominantly between 0.45 and 0.5, indicating high water content for most of the subsurface. Lower Poisson's ratio values are observed at depth below the frying pan and in the first few meters beneath the hill, where lower velocities and higher resistivity exist. Finally, lower Poisson's ratio values are also visible in the shallow subsurface near the end of the profile (300–340 m).

3.3. Rock Physics Modeling

In order to estimate porosity and saturation along the profile, we used a rock physics model based on Hertz-Mindlin contact theory [*Mindlin*, 1949], as formulated by *Helgerud et al.* [1999] and *Helgerud* [2001] and applied to the critical zone by *Holbrook et al.* [2014]. We were able to estimate porosity and saturation distributions in the subsurface from the seismic velocity models by predicting the P and S wave velocities of a mineral aggregate over a range of possible porosities and saturations and finding the porosities and saturations that best match the observed velocities. With this approach, we consider the medium as an aggregate of randomly packed spherical grains and express their bulk elastic properties (i.e., bulk and shear modulus) as functions of the elastic properties of constituent minerals, porosity, saturation, and a critical porosity above which the material properties change from grain-supported to suspension. For each point of our model with defined V_P and V_S values, we performed a grid search on porosities and saturations by using the Hertz-Mindlin rock physics model and looked for the porosities and saturations best fitting both V_P and V_S. After trial and error tests and assuming an altered rhyolitic composition [*Bargar and Muffler*, 1982], the elastic properties of the solid frame were modeled with 40% quartz, 10% feldspar, and 50% clay. Porosity and saturation ranged from 0 to 0.6 and from 0 to 1, respectively, both with a step of 0.025. The root-mean-square errors of the final model were 9 m/s for V_P and 10 m/s for V_S.

The resulting porosity model (Figure 3a) shows that substantial porosity (mostly around 0.5–0.6) exists in the shallow subsurface of this hydrothermal area, consistent with porosities measured on shallow core samples from the area [*Hurwitz et al.*, 2012]. Lower porosities are, however, present at depth below the frying pan and near the NNE end of the line. The predicted saturation model (Figure 3b) shows full saturation for most of the profile with an outcropping water table on both sides of the figure-eight pool. Lower saturation is predicted below the frying pan and in the first few meters of the hill between 70 and 220 m.

4. Discussion

Because seismic velocities and resistivity are sensitive to different physical properties, a comparison between them can provide insight into subsurface structure and gas/water content. The overall low V_P and V_S velocities observed along the line tend to agree with borehole observations of moderately cemented glacial tills in the upper 18 m [*Bargar and Muffler*, 1982]. At shallow depths (<6 m) beneath the hill (from 70 to 220 m), high resistivity, low V_P and V_S, and low Poisson's ratio values can be explained by high-porosity, unsaturated soils, as seen in the rock physics model. Farther to the NNE (from 200 to 340 m), lower resistivities outcrop at the location of the figure-eight pool, consistent with high-temperature, high-solute, and clay-rich hydrothermal fluids feeding the surrounding pools. Although seismic data show a gap in this area, both sides of the figure-eight pool show increasing velocities and Poisson's ratio, consistent with the presence of water. This is well matched by our rock physics model, which shows an increase in water saturation there. Our interpretation also suggests that the high acidity of the water around the figure-eight pool resulting from steam and gas discharge in the pool would increase mineral dissolution of the surrounding rocks and fill the available pore
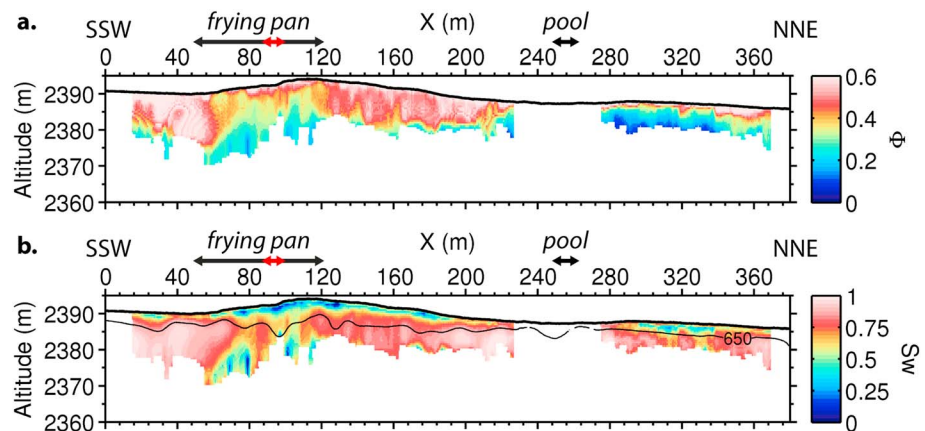
Figure 3. (a) Porosity (Φ) and (b) saturation (S_w) models calculated from seismic velocities by using a Hertz-Mindlin rock physics model, assuming a composition of 40% quartz, 10% feldspar, and 50% clay. The topography extracted from airborne lidar data is represented with a black solid line. The locations of the figure-eight pool and the heat flow anomaly are shown by black arrows, while the active part of the frying pan is indicated by a red arrow. The black contour line in Figure 3b corresponds to a constant V_P of 650 m/s.

space at depth with the derived clays. This is again consistent with our rock physics model, which shows a porosity decrease in this area. The beginning of the line (from 0 to 50 m) is characterized by intermediate resistivity values and high Poisson's ratio, which correspond to a hydrothermally inactive area, partially saturated with fresh water. The area separating the frying pan and the figure-eight pool between 120 and 220 m presents similar characteristics and also appears to be hydrothermally inactive.

Although the frying pan itself is coincident with a shallow resistive area associated with the presence of gas, the main heat flow anomaly surrounding it (between 50 and 120 m) shows strong contrasts of geophysical properties. Notably, this area shows a decrease of V_P but an increase of V_S, suggesting a lower density due to the presence of gas. This observation is highlighted by a strong decrease in Poisson's ratio and is also coincident with low resistivity values at depth, probably originating from the accumulation of clays in the pathways of hydrothermal fluids. These interpretations are in good agreement with the predicted porosity and saturation, which both show a decrease due to the accumulation of clay and the presence of gas. Furthermore, the low predicted saturation values indicate that the phase separation between hydrothermal gas and water occurs at least 15 m deep. Finally, predicted saturations and Poisson's ratio show similar variability, which confirms Poisson's ratio as a reliable underground gas detector in hydrothermal areas. We speculate that weaker degassing areas that are not evident at the surface can be inferred from Poisson's ratio in the NNE part of the profile between 300 and 340 m.

There are several caveats to the hydrothermal interpretations presented here. It is important to keep in mind that the different geophysical techniques used in this study are not affected by the same physical parameters and have different lateral and vertical resolutions. Since electrical methods are mostly sensitive to strong contrasts in electrical resistivity, they might be unable to distinguish gas from water in very conductive clay-rich media. On a second order, these methods are also influenced by temperature variations which could decrease the measured electrical resistivity in the higher heat flow areas. Moreover, P wave velocity models must be viewed as a spatially smoothed version of the real medium, due to ray geometry, inversion regularization, and seismic wavelength. S wave velocities estimated from surface-wave dispersion measurements are, on the contrary, very sensitive to lateral variations when using a sufficiently small extraction window but are less affected by changes of saturation than V_P. As a consequence, the lateral variations of the computed Poisson's ratio, porosity, and saturation models are mainly controlled by V_S, while V_P mostly provides a smoothly varying background velocity. Finally, our geological interpretation is unconstrained by direct sampling via boreholes and assumed a single combination of minerals in the rock physics model. Nevertheless, the proposed interpretation arises from the coupling of resistivity and seismic studies and is consistent with surface observation of degassing and of a local water table outcropping in the pools and the nearby lake, thus highlighting the benefit of using multiple geophysical approaches in the study of shallow hydrothermal systems.

5. Conclusions

We investigated the subsurface architecture of a shallow hydrothermal system in Yellowstone to depths of 15–30 m, using electrical resistivity, *P* wave velocity from refraction data, and *S* wave velocity from surface-wave analysis. Electrical resistivity variations provide robust first-order images of the hydrothermal fluids' flow paths and differentiate hydrothermally active from inactive areas. Poisson's ratio estimated from both *P* and *S* wave velocities shows good sensitivity to variations of saturation, separating the gas-saturated area below the frying pan from the water-saturated areas surrounding it. A rock physics model based on Hertz–Mindlin contact theory validates these qualitative interpretations and provides realistic estimates of porosity and saturation in the subsurface. The predicted porosity distribution shows overall high porosities (0.4–0.6) in the top 10 m of the profile, except below the frying pan and in the NNE side of the figure-eight pool where porosities are lower (0.2–0.4) probably due to clays filling the available pore space. The inferred saturation distribution is consistent with surface observations, showing very low values (<0.25) at the surface of the hill, intermediate values (0.5–0.75) at depth below the frying pan, and high values (>0.75) in the rest of the model, highlighting a local water table outcropping in the pools and the nearby lake. Those results provide critical insight to understand the structure of hydrothermal systems and indicate that the phase separation between hydrothermal fluids occurs at least 15 m in depth. They also illustrate the ability of Poisson's ratio to map the shallow plumbing structure of hydrothermal systems and efficiently constrain gas versus water saturation at depth.

References

Bachrach, R., and P. Avseth (2008), Rock physics modeling of unconsolidated sands: Accounting for nonuniform contacts and heterogeneous stress fields in the effective media approximation with applications to hydrocarbon exploration, *Geophysics*, *73*(6), E197–E209, doi:10.1190/1.2985821.

Bachrach, R., J. Dvorkin, and A. Nur (2000), Seismic velocities and Poisson's ratio of shallow unconsolidated sands, *Geophysics*, *65*(2), 559–564, doi:10.1190/1.1444751.

Bargar, K. E., and L. J. P. Muffler (1982), Hydrothermal alteration in research drill hole Y-11 from a vapor-dominated geothermal system at Mud Volcano, Yellowstone National Park, Wyoming, Thirty-third annual field conference, Wyoming Geological Association guidebook.

Benz, H. M., and R. B. Smith (1984), Simultaneous inversion for lateral velocity variations and hypocenters in the Yellowstone Region using earthquake and refraction data, *J. Geophys. Res.*, *89*(B2), 1208–1220, doi:10.1029/JB089iB02p01208.

Binley, A., and A. Kemna (2005), DC resistivity and induced polarization methods, in *Hydrogeophysics*, pp. 129–156, Springer, Dordrecht, Netherlands.

Boyd, E. S., K. M. Fecteau, J. R. Havig, E. L. Shock, and J. W. Peters (2012), Modeling the habitat range of phototrophs in Yellowstone National Park: Toward the development of a comprehensive fitness landscape, *Front Microbiol*, *3*, doi:10.3389/fmicb.2012.00221.

Bruno, P. P. G., G. P. Ricciardi, Z. Petrillo, V. Di Fiore, A. Troiano, and G. Chiodini (2007), Geophysical and hydrogeological experiments from a shallow hydrothermal system at Solfatara Volcano, Campi Flegrei, Italy: Response to caldera unrest, *J. Geophys. Res.*, *112*, B06201, doi:10.1029/2006JB004383.

Byrdina, S., et al. (2014), Relations between electrical resistivity, carbon dioxide flux, and self-potential in the shallow hydrothermal system of Solfatara (Phlegrean Fields, Italy), *J. Volcanol. Geotherm. Res.*, *283*, 172–182, doi:10.1016/j.jvolgeores.2014.07.010.

Christiansen, R. L. (2001), The Quaternary and Pliocene Yellowstone Plateau volcanic field of Wyoming, Idaho, and Montana, Professional Paper, USGS Numbered Series.

Christiansen, R. L., and H. R. Blank (1975), Geologic map of the Canyon Village quadrangle, Yellowstone National Park, Wyoming, Geologic Quadrangle, USGS Numbered Series.

Chu, R., D. V. Helmberger, D. Sun, J. M. Jackson, and L. Zhu (2010), Mushy magma beneath Yellowstone, *Geophys. Res. Lett.*, *37*, L01306, doi:10.1029/2009GL041656.

Dick, J. M., and E. L. Shock (2011), Calculation of the relative chemical stabilities of proteins as a function of temperature and redox chemistry in a hot spring, *PLoS One*, *6*(8), e22782, doi:10.1371/journal.pone.0022782.

Dick, J. M., and E. L. Shock (2013), A metastable equilibrium model for the relative abundances of microbial phyla in a hot spring, *PLoS One*, *8*(9), e72395, doi:10.1371/journal.pone.0072395.

Dijkstra, E. W. (1959), A note on two problems in connexion with graphs, *Numerische Mathematik*, *1*, 269–271.

Dunkin, J. W. (1965), Computation of modal solutions in layered, elastic media at high frequencies, *Bull. Seismol. Soc. Am.*, *55*(2), 335–358.

Dvorkin, J., and A. Nur (1996), Elasticity of high-porosity sandstones: Theory for two North Sea data sets, *Geophysics*, *61*(5), 1363–1370, doi:10.1190/1.1444059.

Dvorkin, J., and A. Nur (1998), Acoustic signatures of patchy saturation, *Int. J. Solids Struct.*, *35*(34–35), 4803–4810, doi:10.1016/S0020-7683(98)00095-X.

Farrell, J., R. B. Smith, S. Husen, and T. Diehl (2014), Tomography from 26 years of seismicity revealing that the spatial extent of the Yellowstone crustal magma reservoir extends well beyond the Yellowstone caldera, *Geophys. Res. Lett.*, *41*, 3068–3073, doi:10.1002/2014GL059588.

Finizola, A., et al. (2010), Adventive hydrothermal circulation on Stromboli volcano (Aeolian Islands, Italy) revealed by geophysical and geochemical approaches: Implications for general fluid flow models on volcanoes, *J. Volcanol. Geotherm. Res.*, *196*(1–2), 111–119, doi:10.1016/j.jvolgeores.2010.07.022.

Fournier, R. O. (1989), Geochemistry and dynamics of the Yellowstone National Park hydrothermal system, *Annu. Rev. Earth Planet. Sci.*, *17*(1), 13–53, doi:10.1146/annurev.ea.17.050189.000305.

Gassmann, F. (1951), Elasticity of porous media: Über die Elastizität poröser Medien, *Vierteljahrsschrift der Naturforschenden Gesellschaft*, *96*, 1–23.

Gibson, M. L., and N. W. Hinman (2013), Mixing of hydrothermal water and groundwater near hot springs, Yellowstone National Park (USA): Hydrology and geochemistry, *Hydrogeol. J.*, *21*(4), 919–933, doi:10.1007/s10040-013-0965-4.

Haskell, N. A. (1953), The dispersion of surface waves on multilayered media, *Bull. Seismol. Soc. Am.*, *43*(1), 17–34.

Heenan, J., L. Slater, D. Ntarlagiannis, E. Atekwana, B. Fathepure, S. Dalvi, C. Ross, D. Werkema, and E. Atekwana (2014), Electrical resistivity imaging for long-term autonomous monitoring of hydrocarbon degradation: Lessons from the Deepwater Horizon oil spill, *Geophysics*, *80*(1), B1–B11, doi:10.1190/geo2013-0468.1.

Helgerud, M. B. (2001), Wave speeds in gas hydrate and sediments containing gas hydrate: A laboratory and modeling study, PhD thesis, Stanford Univ.

Helgerud, M. B., J. Dvorkin, A. Nur, A. Sakai, and T. Collett (1999), Elastic-wave velocity in marine sediments with gas hydrates: Effective medium modeling, *Geophys. Res. Lett.*, *26*(13), 2021–2024, doi:10.1029/1999GL900421.

Hill, R. (1952), The elastic behaviour of a crystalline aggregate, *Proc. Phys. Soc. A*, *65*(5), 349–354, doi:10.1088/0370-1298/65/5/307.

Holbrook, W. S., C. S. Riebe, M. Elwaseif, J. L. Hayes, K. Basler-Reeder, D. L. Harry, A. Malazian, A. Dosseto, P. C. Hartsough, and J. W. Hopmans (2014), Geophysical constraints on deep weathering and water storage potential in the Southern Sierra Critical Zone Observatory, *Earth Surf. Process. Landforms*, *39*(3), 366–380, doi:10.1002/esp.3502.

Huang, H.-H., F.-C. Lin, B. Schmandt, J. Farrell, R. B. Smith, and V. C. Tsai (2015), The Yellowstone magmatic system from the mantle plume to the upper crust, *Science*, *348*(6236), 773–776, doi:10.1126/science.aaa5648.

Hurwitz, S., and J. B. Lowenstern (2014), Dynamics of the Yellowstone hydrothermal system, *Rev. Geophys.*, *52*, doi:10.1002/2014RG000452.

Hurwitz, S., J. B. Lowenstern, and H. Heasler (2007), Spatial and temporal geochemical trends in the hydrothermal system of Yellowstone National Park: Inferences from river solute fluxes, *J. Volcanol. Geotherm. Res.*, *162*(3–4), 149–171, doi:10.1016/j.jvolgeores.2007.01.003.

Hurwitz, S., R. N. Harris, C. A. Werner, and F. Murphy (2012), Heat flow in vapor dominated areas of the Yellowstone Plateau Volcanic Field: Implications for the thermal budget of the Yellowstone Caldera, *J. Geophys. Res.*, *117*, B10207, doi:10.1029/2012JB009463.

Husen, S., R. B. Smith, and G. P. Waite (2004), Evidence for gas and magmatic sources beneath the Yellowstone volcanic field from seismic tomographic imaging, *J. Volcanol. Geotherm. Res.*, *131*(3–4), 397–410, doi:10.1016/S0377-0273(03)00416-5.

Johansen, T., E. Jensen, G. Mavko, and J. Dvorkin (2013), Inverse rock physics modeling for reservoir quality prediction, *Geophysics*, *78*(2), M1–M18, doi:10.1190/geo2012-0215.1.

Koestel, J., A. Kemna, M. Javaux, A. Binley, and H. Vereecken (2008), Quantitative imaging of solute transport in an unsaturated and undisturbed soil monolith with 3-D ERT and TDR, *Water Resour. Res.*, *44*, W12411, doi:10.1029/2007WR006755.

Lowenstern, J. B., and S. Hurwitz (2008), Monitoring a supervolcano in repose: Heat and volatile flux at the Yellowstone caldera, *Elements*, *4*(1), 35–40, doi:10.2113/GSELEMENTS.4.1.35.

Lowenstern, J. B., D. Bergfeld, W. C. Evans, and S. Hurwitz (2012), Generation and evolution of hydrothermal fluids at Yellowstone: Insights from the Heart Lake Geyser Basin, *Geochem. Geophys. Geosyst.*, *13*, Q01017, doi:10.1029/2011GC003835.

Mavko, G., T. Mukerji, and J. Dvorkin (2003), *The Rock Physics Handbook: Tools for Seismic Analysis of Porous Media*, Cambridge Univ. Press, Cambridge, U. K.

Matthews, N. E., J. A. Vazquez, and A. T. Calvert (2015), Age of the Lava Creek supereruption and magma chamber assembly at Yellowstone based on 40Ar/39Ar and U-Pb dating of sanidine and zircon crystals, *Geochem. Geophys. Geosyst.*, *16*, 2508–2528, doi:10.1002/2015GC005881.

Meyer-Dombard, D. R., E. L. Shock, and J. P. Amend (2005), Archaeal and bacterial communities in geochemically diverse hot springs of Yellowstone National Park, USA, *Geobiology*, *3*(3), 211–227, doi:10.1111/j.1472-4669.2005.00052.x.

Miller, D. S., and R. B. Smith (1999), P and S velocity structure of the Yellowstone volcanic field from local earthquake and controlled-source tomography, *J. Geophys. Res.*, *104*(B7), 15,105–15,121, doi:10.1029/1998JB900095.

Mindlin, R. D. (1949), Compliance of elastic bodies in contact, *J. Appl. Mech.*, *16*, 259–268.

Mokhtar, T. A., R. B. Herrmann, and D. R. Russell (1988), Seismic velocity and Q model for the shallow structure of the Arabian Shield from short-period Rayleigh waves, *Geophysics*, *53*(11), 1379–1387, doi:10.1190/1.1442417.

Morgan, L. A., and W. C. Shanks (2005), Influences of rhyolitic lava flows on hydrothermal processes in Yellowstone Lake and on the Yellowstone Plateau, in *Geothermal Biology and Geochemistry in Yellowstone National Park*, edited by W. P. Inskeep and T. R. McDermott, pp. 31–52, Montana State Univ. Publications, Bozeman, Mont.

Moser, T. (1991), Shortest path calculation of seismic rays, *Geophysics*, *56*(1), 59–67, doi:10.1190/1.1442958.

Neducza, B. (2007), Stacking of surface waves, *Geophysics*, *72*(2), 51–58, doi:10.1190/1.2431635.

Nur, A., G. Mavko, J. Dvorkin, and D. Galmudi (1998), Critical porosity: A key to relating physical properties to porosity in rocks, *The Leading Edge*, *17*(3), 357–362, doi:10.1190/1.1437977.

Oldenburg, D. W., and Y. Li (1999), Estimating depth of investigation in DC resistivity and IP surveys, *Geophysics*, *64*(2), 403, doi:10.1190/1.1444545.

O'Neill, A. (2003), Full-waveform reflectivity for modelling, inversion and appraisal of seismic surface wave dispersion in shallow site investigations, Univ. of Western Australia, Perth, Australia.

O'Neill, A., M. Dentith, and R. List (2003), Full-waveform P-SV reflectivity inversion of surface waves for shallow engineering applications, *Explor. Geophys.*, *34*(3), 158–173.

Pasquet, S., and L. Bodet (2016), Integrated workflow for surface-wave dispersion inversion and profiling, in *Near Surface Geoscience 2016— 22nd European Meeting of Environmental and Engineering Geophysics*, EAGE, Barcelona, Spain.

Pasquet, S., L. Bodet, A. Dhemaied, A. Mouhri, Q. Vitale, F. Rejiba, N. Flipo, and R. Guérin (2015a), Detecting different water table levels in a shallow aquifer with combined P-, surface and SH-wave surveys: Insights from VP/VS or Poisson's ratios, *J. Appl. Geophys.*, *113*, 38–50, doi:10.1016/j.jappgeo.2014.12.005.

Pasquet, S., L. Bodet, L. Longuevergne, A. Dhemaied, C. Camerlynck, F. Rejiba, and R. Guérin (2015b), 2D characterization of near-surface VP/VS: Surface-wave dispersion inversion versus refraction tomography, *Near Surf. Geophys.*, *13*(4), 315–331, doi:10.3997/1873-0604.2015028.

Revil, A., A. Finizola, F. Sortino, and M. Ripepe (2004), Geophysical investigations at Stromboli volcano, Italy: Implications for ground water flow and paroxysmal activity, *Geophys. J. Int.*, *157*(1), 426–440, doi:10.1111/j.1365-246X.2004.02181.x.

Revil, A., et al. (2008), Inner structure of La Fossa di Vulcano (Vulcano Island, southern Tyrrhenian Sea, Italy) revealed by high-resolution electric resistivity tomography coupled with self-potential, temperature, and CO2 diffuse degassing measurements, *J. Geophys. Res.*, *113*, B07207, doi:10.1029/2007JB005394.

Rosas-Carbajal, M., J.-C. Komorowski, F. Nicollin, and D. Gibert (2016), Volcano electrical tomography unveils edifice collapse hazard linked to hydrothermal system structure and dynamics, *Sci. Rep.*, *6*, 29,899, doi:10.1038/srep29899.

Sambridge, M. (1999), Geophysical inversion with a neighbourhood algorithm—I. Searching a parameter space, *Geophys. J. Int.*, *138*(2), 479–494, doi:10.1046/j.1365-246X.1999.00876.x.

Shock, E. L., M. Holland, D. Meyer-Dombard, and J. P. Amend (2005), Geochemical sources of energy for microbial metabolism in hydrothermal ecosystems: Obsidian Pool, Yellowstone National Park, in *Geothermal Biology and Geochemistry in Yellowstone National Park*, edited by W. P. Inskeep and T. R. McDermott, pp. 95–110, Thermal Biol. Inst., Mont. State Univ., Bozeman.

Slater, L., A. M. Binley, W. Daily, and R. Johnson (2000), Cross-hole electrical imaging of a controlled saline tracer injection, *J. Appl. Geophys.*, *44*(2–3), 85–102, doi:10.1016/S0926-9851(00)00002-1.

St. Clair, J. (2015), Geophysical investigations of underplating at the Middle American Trench, weathering in the critical zone, and snow water equivalent in seasonal snow, PhD thesis, Univ. of Wyoming.

St. Clair, J., S. Moon, W. S. Holbrook, J. T. Perron, C. S. Riebe, S. J. Martel, B. Carr, C. Harman, K. Singha, and D. Richter (2015), Geophysical imaging reveals topographic stress control of bedrock weathering, *Science*, *350*(6260), 534–538, doi:10.1126/science.aab2210.

Thomson, W. T. (1950), Transmission of elastic waves through a stratified solid medium, *J. Appl. Phys.*, *21*(2), 89–93, doi:10.1063/1.1699629.

Vandemeulebrouck, J., P. Roux, and E. Cros (2013), The plumbing of Old Faithful Geyser revealed by hydrothermal tremor, *Geophys. Res. Lett.*, *40*, 1989–1993, doi:10.1002/grl.50422.

Vandemeulebrouck, J., et al. (2014), Eruptions at Lone Star geyser, Yellowstone National Park, USA: 2. Constraints on subsurface dynamics, *J. Geophys. Res. Solid Earth*, *119*, 8688–8707, doi:10.1002/2014JB011526.

Vitale, M. V., P. Gardner, and N. W. Hinman (2008), Surface water–groundwater interaction and chemistry in a mineral-armored hydrothermal outflow channel, Yellowstone National Park, USA, *Hydrogeol. J.*, *16*(7), 1381–1393, doi:10.1007/s10040-008-0344-8.

Wathelet, M., D. Jongmans, and M. Ohrnberger (2004), Surface-wave inversion using a direct search algorithm and its application to ambient vibration measurements, *Near Surf. Geophys.*, *2*(4), 211–221, doi:10.3997/1873-0604.2004018.

Werner, C., and S. Brantley (2003), CO_2 emissions from the Yellowstone volcanic system, *Geochem. Geophys. Geosyst.*, *4*(7), 1061, doi:10.1029/2002GC000473.

Werner, C., S. L. Brantley, and K. Boomer (2000), CO_2 emissions related to the Yellowstone volcanic system: 2. Statistical sampling, total degassing, and transport mechanisms, *J. Geophys. Res.*, *105*(B5), 10,831–10,846, doi:10.1029/1999JB900331.

White, D. E., L. J. P. Muffler, and A. H. Truesdell (1971), Vapor-dominated hydrothermal systems compared with hot-water systems, *Econ. Geol.*, *66*(1), 75–97, doi:10.2113/gsecongeo.66.1.75.

Zohdy, A. A. R., L. A. Anderson, and L. J. P. Muffler (1973), Resistivity, self-potential, and induced-polarization surveys of a vapor-dominated geothermal system, *Geophysics*, *38*(6), 1130–1144, doi:10.1190/1.1440400.